

Time-domain finite-difference modeling for attenuative anisotropic media

Tong Bai¹ and Ilya Tsvankin¹

ABSTRACT

Accurate and efficient modeling of seismic wavefields that accounts for both attenuation and anisotropy is essential for further development of processing methods. Here, we present a 2D time-domain finite-difference algorithm for generating multicomponent data in viscoelastic transversely isotropic media with a vertical symmetry axis (VTI). Within the framework of the generalized standard linear solid (GSLs) model, the relaxation function is expressed through the τ -parameters (which quantify the difference between the stress and strain relaxation times) defined for anisotropic media. This approach produces nearly constant values of all components of the quality-factor matrix within a specified frequency band. The developed algorithm is based on a set of anisotropic viscoelastic wave equations parameterized by memory variables. Synthetic examples for TI models with different structural complexity confirm the accuracy of the proposed scheme and illustrate the influence of attenuation and attenuation anisotropy on multicomponent wavefields.

INTRODUCTION

Viscoelastic properties of subsurface formations have a profound influence on wave propagation and seismic processing. The attenuation-induced amplitude loss and velocity dispersion can cause distortions in amplitude-variation-with-offset (AVO) analysis and imaging. However, attenuation can also provide valuable information about lithology and fluids needed for reservoir characterization.

A prerequisite for accurate attenuation analysis and estimation is efficient viscoelastic modeling (e.g., Shekar and Tsvankin, 2014). The main advantage of finite-difference (FD) methods compared to asymptotic algorithms is their ability to simulate the complete wavefield without sacrificing accuracy. In frequency-domain mod-

eling, attenuation can be incorporated directly through the imaginary part of the stiffness coefficients. However, implementation of finite-difference methods in the frequency domain is hampered by the need to factorize a large sparse linear system of equations (Operto et al., 2007). As a result, many publications are focused on simulating wave propagation in attenuative media with finite-difference time-domain methods (Day and Minster, 1984; Emmerich and Korn, 1987; Carcione, 1993; Blanch et al., 1995; Bohlen, 2002; Zhu et al., 2013). A nearly constant quality factor Q over a specified frequency range can be simulated by mechanical models. Memory variables, introduced into the corresponding convolutional stress-strain relationship, facilitate numerical implementation (Robertsson et al., 1994).

The attenuation coefficient for subsurface formations is often directionally dependent, and the magnitude of attenuation anisotropy is typically much higher than that of velocity anisotropy (Hosten et al., 1987; Zhu and Tsvankin, 2006; Behura and Tsvankin, 2009a). Červený (2005) and Vavryčuk (2007) present a detailed discussion of attenuation anisotropy based on ray theory. Behura and Tsvankin (2009b) show that the attenuation coefficient along seismic rays is close to the corresponding phase attenuation coefficient (computed for zero “inhomogeneity angle”) even for strong anisotropy. Shekar and Tsvankin (2014) develop an efficient Kirchhoff modeling algorithm for attenuative anisotropic media using Gaussian beams.

Although time-domain viscoelastic wave equations for general anisotropic media have been known for a long time (e.g., Tarantola, 1988; Komatitsch and Tromp, 1999; Charara et al., 2000; Fichtner and van Driel, 2014), they were considered “too general for seismic purposes” (Tarantola, 1988) and thus seldom implemented. In one of the few published attempts to include attenuation anisotropy in time-domain FD modeling, Mittet and Renlie (1996) simulate acoustic full-waveform multipole logging. However, they do not give a clear description of employed attenuation anisotropy.

Here, we develop a 2D time-domain FD algorithm designed to simulate P- and SV-waves for models with VTI symmetry for both velocity and attenuation. First, we discuss the rheology of an anisotropic viscoelastic model and a formalism for generating nearly

Manuscript received by the Editor 7 August 2015; revised manuscript received 6 November 2015; published online 18 March 2016.

¹Center for Wave Phenomena, Colorado School of Mines, Golden, Colorado, USA. E-mail: tbai@mines.edu; ilya@mines.edu.

© 2016 Society of Exploration Geophysicists. All rights reserved.

constant Q_{ij} -values in a specified frequency band. Next, we present the viscoelastic wave equation for VTI media and describe its implementation in FD modeling. Finally, we demonstrate the accuracy and efficiency of the developed FD algorithm with numerical examples.

METHODOLOGY

Rheology of anisotropic viscoelastic model

The stiffness matrix C_{ij} in viscoelastic media becomes complex, and attenuation can be described by the quality-factor matrix Q_{ij} (Zhu and Tsvankin, 2006; Carcione, 2007):

$$Q_{ij} = \frac{\text{Re}(C_{ij})}{\text{Im}(C_{ij})}. \quad (1)$$

Attenuation can be easily incorporated into frequency-domain modeling through the imaginary parts of the stiffnesses or through the matrix Q_{ij} (Operto et al., 2009; Gosselin-Cliche and Giroux, 2014; Shekar and Tsvankin, 2014). In the time domain, however, attenuation is typically introduced through the so-called relaxation function Ψ (Carcione, 2007; Moczo et al., 2007):

$$\Psi_{ij}(t) = F^{-1} \left\{ \frac{C_{ij}(\omega)}{i\omega} \right\}, \quad (2)$$

where F^{-1} denotes the inverse Fourier transform, and both Ψ_{ij} and C_{ij} are expressed in the two-index Voigt notation. The generalized stress-strain relationship in linear viscoelastic media can be written as:

$$\sigma_{mn} = \Psi_{mnpq} * \dot{\varepsilon}_{pq} = \dot{\Psi}_{mnpq} * \varepsilon_{pq}, \quad (3)$$

where σ_{mn} and ε_{pq} are the stress and strain tensor, respectively, and the asterisk and dot denote convolution and time derivative, respectively. Equation 3 shows that the stress tensor depends on the entire history of the strain field, rather than by just its current value (which is the case for purely elastic media).

The relaxation function, which determines the viscoelastic behavior of the material, can be simulated by the so-called generalized standard linear solid (GSLs) model. A single standard linear solid (SLS) consists of two parallel mechanical systems, with one made of a spring and a dashpot in series and the other containing a single spring (Blanch et al., 1995). Several SLS's in parallel constitute the GSLs, with each individual SLS called a "relaxation mechanism." Most existing publications implement a relaxation function for isotropic media (e.g., Carcione, 1993; Moczo et al., 2007). For general anisotropic media, the function Ψ_{ij} is given by (Komatitsch and Tromp, 1999; Charara et al., 2000):

$$\Psi_{ij}(t) = C_{ij}^R \left[1 - \frac{1}{L} \sum_{l=1}^L \left(1 - \frac{\tau_{ij}^{el}}{\tau^{\sigma l}} \right) e^{-t/\tau^{\sigma l}} \right] H(t), \quad (4)$$

where $C_{ij}^R = \Psi_{ij}(t \rightarrow \infty)$ is called the "relaxed modulus" corresponding to the low-frequency limit ($\omega = 0$), τ_{ij}^{el} and $\tau^{\sigma l}$ are the strain and stress relaxation times (respectively) for the l th mechanism, $H(t)$

is the Heaviside function, and L is the number of mechanisms. The relaxed modulus C_{ij}^R is related to the real part of the corresponding complex modulus C_{ij} defined at the reference frequency ω_r :

$$C_{ij}^R = \text{Re}(C_{ij}) \left[\frac{1}{L} \sum_{l=1}^L \frac{1 + \omega_r^2 \tau^{\sigma l} \tau_{ij}^{el}}{1 + (\omega_r \tau^{\sigma l})^2} \right]^{-1}. \quad (5)$$

Generally, the more relaxation mechanisms (or SLSs) are included, the wider is the frequency range in which it is possible to simulate a nearly constant Q_{ij} . For different components of the anisotropic relaxation tensor Ψ , the stress relaxation times can be identical, while τ_{ij}^{el} generally differ (Komatitsch and Tromp, 1999).

The τ -method

Blanch et al. (1995) demonstrate that the magnitude of attenuation in isotropic media is directly determined by the dimensionless parameter τ :

$$\tau = \frac{\tau^{el}}{\tau^{\sigma l}} - 1. \quad (6)$$

For anisotropic media, τ becomes a matrix that we define as:

$$\tau_{ij} = \frac{\tau_{ij}^{el}}{\tau^{\sigma l}} - 1. \quad (7)$$

The quality-factor elements Q_{ij} decrease with increasing τ_{ij} . In the elastic case, the stress and strain relaxation times are equal, and τ_{ij} vanishes. Since τ_{ij} should remain constant for all relaxation mechanisms, the number of independent parameters (τ_{ij} and $\tau^{\sigma l}$) for each element of the relaxation function Ψ_{ij} reduces from $2L$ to $L + 1$ (L denotes the number of relaxation mechanisms). For P- and SV-waves in a 2D viscoelastic VTI model, the total number of independent parameters is equal to $L + 4$ (L for $\tau^{\sigma l}$ and 4 for τ_{ij}).

The expressions for the relaxation function (equation 4) and τ_{ij} (equation 7) allow us to find the complex modulus C_{ij} from equation 2. Then the inverse of the quality factor is given by

$$Q_{ij}^{-1}(\omega) = \frac{\text{Im}(C_{ij})}{\text{Re}(C_{ij})} = \frac{\tau_{ij} \sum_{l=1}^L \frac{\omega \tau^{\sigma l}}{1 + (\omega \tau^{\sigma l})^2}}{L + \tau_{ij} \sum_{l=1}^L \frac{(\omega \tau^{\sigma l})^2}{1 + (\omega \tau^{\sigma l})^2}}. \quad (8)$$

By applying least-squares inversion to equation 8, we can obtain the corresponding parameters τ_{ij} and $\tau^{\sigma l}$, which produce the desired nearly constant value of Q_{ij} in a specified frequency band (Bohlen, 2002). Figure 1 shows that the simulated Q_{ij} -curve using the inverted parameters $\tau^{\sigma l}$ and τ_{ij} is close to the desired Q_{ij} -value, when three relaxation mechanisms are used.

Viscoelastic VTI wave equation and FD implementation

Using equations 3, 4, and 7, the viscoelastic constitutive relation for 2D VTI media can be obtained as (Appendix A; Tromp et al., 2005; Fichtner and van Driel, 2014):

$$\dot{\sigma}_{mn} = \frac{1}{2} C_{mnpq}^U (v_{p,q} + v_{q,p}) + \sum_{l=1}^L r_{mn}^l, \quad (9)$$

and

$$i_{mn}^l = -\frac{1}{\tau_{\sigma l}} \left[\frac{1}{2L} (C_{mnpq}^U - C_{mnpq}^R) (v_{p,q} + v_{q,p}) + r_{mn}^l \right], \quad (10)$$

where $v_{p,q}$ is the derivative of the p th component of the particle velocity with respect to x_q , C_{mnpq}^R are the relaxed moduli, C_{mnpq}^U are the unrelaxed moduli defined as $C_{mnpq}^U = C_{mnpq}^R (1 + \tau_{mnpq})$, and r_{mn}^l are the memory variables for the l th mechanism. The Einstein summation convention over p and q ($p = 1,3; q = 1,3$) is assumed, and $mn = 11, 13, 33$; C_{mnpq}^U and C_{mnpq}^R can be expressed in the two-index notation using Voigt convention.

Equations 9 and 10 plus the momentum conservation law constitute the viscoelastic VTI wave equation, which allows us to carry out time-domain FD modeling for media with VTI symmetry for both velocity and attenuation. The stress-velocity formulation is adopted here because of its natural connection to staggered grids (Moczo et al., 2007), which generally provide high numerical accuracy. Our algorithm is based on a rotated staggered grid (RSG) (Saenger et al., 2000; Saenger and Bohlen, 2004, see Figure 2), which is preferable to the standard staggered grid (SSG) in anisotropic media. The particle velocity and density are defined at the center of each cell (staggered grid point), while other parameters including stress, memory variables, stress relaxation time, and τ_{ij} are assigned to regular grid points. The two sets of parameters are related through FD operators in the auxiliary directions \tilde{x} and \tilde{z} , as discussed by Saenger et al. (2000).

The time and spatial derivatives are approximated by the second-order and 12th-order centered differences, respectively, with the time derivative calculated using the leap-frog scheme (Kristek and Moczo, 2003). A sponge-layer absorbing boundary condition is applied to eliminate reflections from the model boundaries. To minimize numerical artifacts and avoid instabilities, we apply spatial and temporal sampling criteria modified after Bohlen (2002):

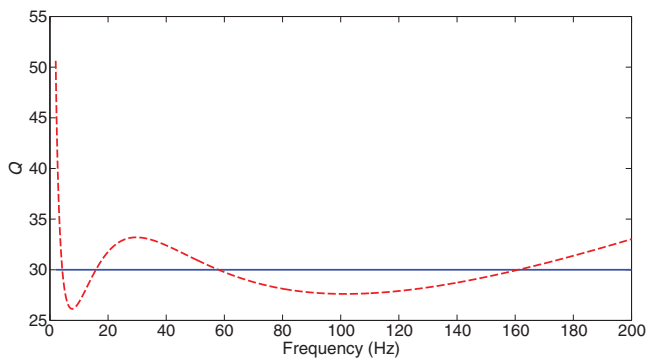


Figure 1. Curve of Q_{ij} (dashed line) simulated with three relaxation mechanisms in the frequency range from 2 to 200 Hz. The desired value of Q_{ij} is 30 (solid line). The inverted parameters are: $\tau_{ij} = 0.2124$, $\tau^{\sigma 1} = 22.7$ ms, $\tau^{\sigma 2} = 1.3$ ms, and $\tau^{\sigma 3} = 2 \times 10^{-3}$ ms.

$$dh \leq \frac{\lambda_{\min}}{n} = \frac{V_{S,\min}}{n f_{\max}} \quad (11)$$

and

$$dt \leq \frac{dh}{\sqrt{2m} V_{P,\max}}, \quad (12)$$

where λ_{\min} denotes the minimum wavelength, $V_{S,\min}$ and $V_{P,\max}$ are the smallest S-wave velocity and largest P-wave velocity (taking into account anisotropy and dispersion), f_{\max} is the maximum frequency in the source spectrum, and n and m are empirical parameters determined by the type and order of the FD scheme. In particular, m can be approximated by the sum of the absolute values of the FD coefficients. For our algorithm, these parameters are set as $n = 3$ and $m = 1.37$.

Velocity dispersion

Physical dispersion refers to the velocity variation with frequency, which should be distinguished from numerical dispersion caused by discretization in FD computations. Attenuative media have to be dispersive to ensure causality (Futterman, 1962; Jacobson, 1987; Sun et al., 2009). In the GSLS model, the frequency-dependent P-wave vertical velocity for VTI media takes the form:

$$V_{P0}(\omega) = \sqrt{\frac{\text{Re}(C_{33}(\omega))}{\rho}} = \sqrt{\frac{C_{33}^R}{\rho} \left[1 + \frac{\tau_{33}}{L} \sum_{l=1}^L \frac{(\omega \tau^{\sigma l})^2}{1 + (\omega \tau^{\sigma l})^2} \right]}, \quad (13)$$

where $C_{33}(\omega)$ is the complex modulus and C_{33}^R is the relaxed modulus defined in equation 5.

Figure 3 displays the dispersion curves of the GSLS model with three relaxation mechanisms and of the constant- Q model of Kjartansson (1979; see Carcione, 2007). The velocity in viscoelastic media is higher than the reference value for frequencies exceeding ω_r ; for lower frequencies, the opposite is true.

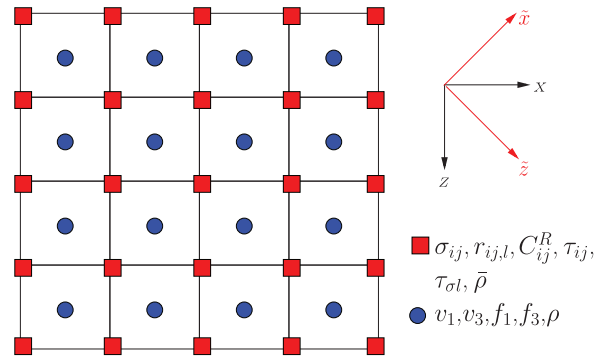


Figure 2. Scheme of a rotated staggered grid (RSG).

SYNTHETIC EXAMPLES

Validation test

To check the accuracy of the developed FD algorithm, we apply it to generate the wavefield in a two-layer viscoelastic VTI medium and then estimate the P-wave attenuation coefficient with the spectral-ratio method.

Using the vertical component of the reflection data generated for the model in Figure 4 and Table 1, we pick the PP events at different receiver locations and then obtain the frequency spectrum $U^{(1)}(\omega)$ of these arrivals. Similarly, we estimate the corresponding spectrum $U^{(0)}(\omega)$ for the reference elastic medium. Then, according to the spectral-ratio method (Zhu et al., 2007; Behura and Tsvankin, 2009a), the logarithm of the frequency-domain amplitude ratio can be expressed as

$$\ln \left| \frac{U^{(1)}(\omega)}{U^{(0)}(\omega)} \right| = G - 2\pi A_P f t, \quad (14)$$

where G , which is assumed to be frequency-independent, accounts for the source radiation pattern, geometric spreading, and reflection/transmission coefficients, t is the travelttime, and A_P is the P-wave

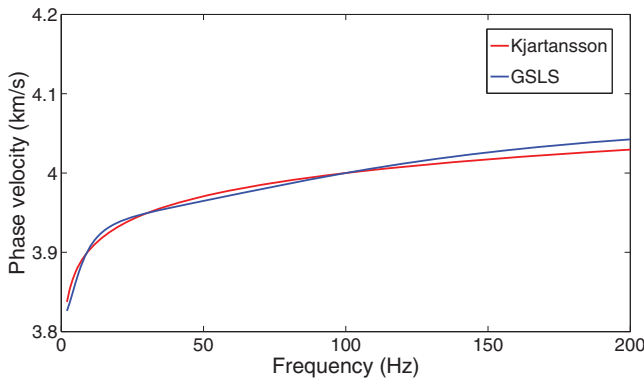


Figure 3. Dispersion curves of the GSLS model with three relaxation mechanisms and of Kjartansson's constant- Q model, with $Q = 30$ in both cases. The reference velocity is 4 km/s at a frequency of 100 Hz.

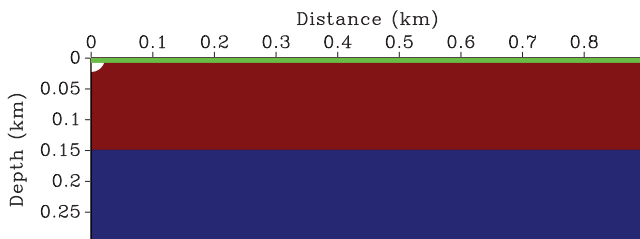


Figure 4. Two-layer VTI model used for attenuation estimation. The model size is $900 \text{ m} \times 300 \text{ m}$, with grid spacing $\Delta x = \Delta z = 3 \text{ m}$. A horizontal reflector is located at a depth of 150 m. In the first layer, $V_{P0} = 3.0 \text{ km/s}$, $V_{S0} = 1.5 \text{ km/s}$, $\rho = 2.0 \text{ g/m}^3$, $\epsilon = 0.2$, and $\delta = 0.1$; in the second layer, $V_{P0} = 2.0 \text{ km/s}$, $V_{S0} = 1.0 \text{ km/s}$, $\rho = 2.0 \text{ g/m}^3$, $\epsilon = 0.15$, and $\delta = 0.05$. The attenuation parameters are the same for both layers and are listed in the first row of Table 1. An explosive source that excites a Ricker wavelet with a central frequency of 100 Hz is placed at the origin (white dot). The green line marks the receiver locations at the surface.

group attenuation coefficient. As shown by Behura and Tsvankin (2009b), the coefficient A_P is equal to the phase attenuation coefficient [which can be represented as $1/(2Q_P)$] computed for zero inhomogeneity angle (the angle between the real and imaginary parts of the wave vector).

Hence, the slope of the logarithmic spectral ratio yields the product $2\pi A_P t$. Figure 5 shows that the slope remains almost constant in a wide frequency range, as expected for a frequency-independent Q model. Some deviations from a straight line at high frequencies can be explained by the fact that we simulated a nearly constant- Q_{ij} in the frequency band from 2 to 200 Hz. After applying the spectral-ratio method at different offsets, we invert for the attenuation parameters A_{P0} , ϵ_Q , and δ_Q using the following linearized expression for the coefficient A_P (Zhu and Tsvankin, 2006):

$$A_P(\theta) = A_{P0}(1 + \delta_Q \sin^2 \theta \cos^2 \theta + \epsilon_Q \sin^4 \theta), \quad (15)$$

where θ is the phase angle with the symmetry axis, A_{P0} is the P-wave vertical phase attenuation coefficient [close to $1/(2Q_{P0})$ for weak attenuation], ϵ_Q is the anisotropy parameter that quantifies the fractional difference between the horizontal and vertical attenuation coefficients, and δ_Q controls the curvature of $A_P(\theta)$ in the vertical direction. The attenuation-anisotropy parameters are defined as (Zhu and Tsvankin, 2006):

$$\epsilon_Q = \frac{Q_{33} - Q_{11}}{Q_{11}}, \quad (16)$$

$$\delta_Q = \frac{1}{2A_{P0}} \left. \frac{d^2 A_P}{d\theta^2} \right|_{\theta=0^\circ}. \quad (17)$$

Table 1. Actual and estimated attenuation parameters for the two-layer model from Figure 4. The quality factor Q_{S0} was not estimated in this test because it requires special processing of mode-converted data (see Shekar and Tsvankin, 2011).

	Q_{P0}	Q_{S0}	ϵ_Q	δ_Q
Actual	30	30	0.4	1.2
Estimated	32.4	—	0.3	1.1

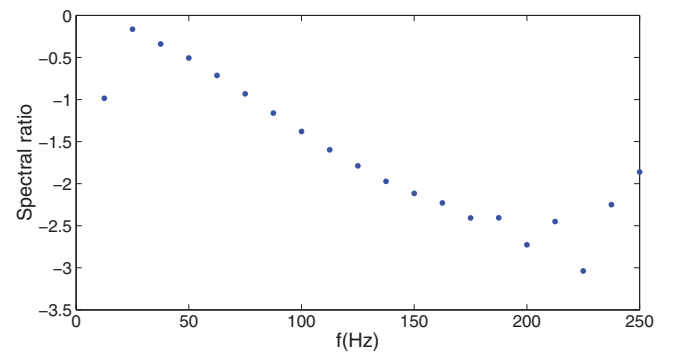


Figure 5. Logarithm of the amplitude ratio versus frequency for the PP reflection at an offset of 210 m (phase angle is about 28°) in the model from Figure 4.

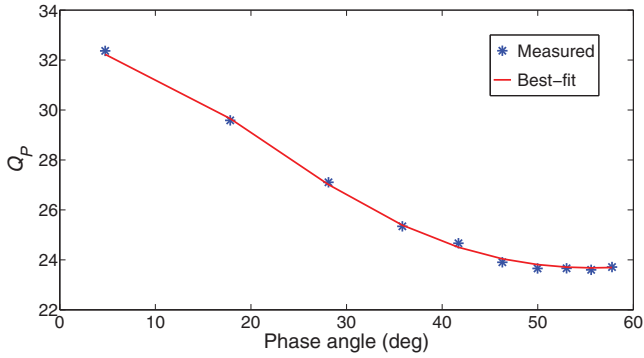


Figure 6. P-wave quality factors obtained from the spectral-ratio method (stars) and the best-fit linearized approximation (equation 15, solid line).

We process reflections in the offset range from 30 m to 840 m with an increment of 90 m and estimate the corresponding phase angles from the group angles using a linearized relationship (Tsvankin, 2012).

The inverted parameters, listed in the second row of Table 1, accurately reproduce the angle-dependent P-wave attenuation coefficient (Figure 6). The small discrepancies between the actual and inverted parameters in Table 1 are likely caused by the linearized approximations for the phase angle and the attenuation coefficient (equation 15), as well as by the deviations of the simulated Q_{ij} from the desired constant value. The inversion results can be further improved by using the exact attenuation coefficients obtained from the Christoffel equation (Zhu and Tsvankin, 2006; Carcione, 2007).

Examples for attenuative VTI models

Here, we present three modeling experiments to illustrate the performance of the algorithm and the influence of attenuation anisotropy. The snapshots of the amplitude of the particle velocity for a homogeneous VTI model are shown in Figure 7a–7d. Compared to the wavefield for a nonattenuative medium in Figure 7a, the P- and SV-arrivals in Figure 7b–7d exhibit clearly visible amplitude decay due to attenuation and attenuation anisotropy. The contribution of the coefficient ϵ_Q in equation 15, in accordance with its definition, increases toward the isotropy (horizontal) plane (Figure 7d and 7f). The parameter δ_Q controls the angular variation of the P-wave attenuation coefficient near the vertical direction (Zhu and Tsvankin, 2006), so its influence is visible mostly at intermediate propagation angles (Figure 7c and 7e). Note that the SV-wave attenuation anisotropy is largely controlled by the parameter σ_Q (which is a function of $\epsilon_Q - \delta_Q$, see the expression in Zhu and Tsvankin, 2006), which is

negative in Figure 7c and positive in Figure 7d. When σ_Q is negative, the SV-wave attenuation coefficient decreases in the range of phase angles from 0° to 45° and then increases from 45° to 90° (Figure 7c and 7e); for positive σ_Q , the opposite is true (Figure 7d and 7f).

Next, the three-layer model from Table 2 is used to simulate reflection data in the presence of attenuation anisotropy. We com-

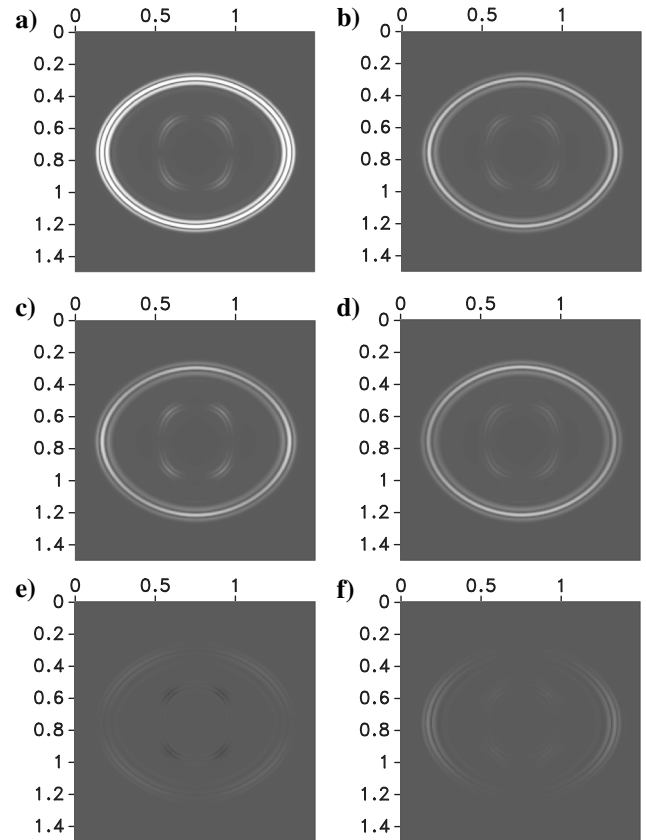


Figure 7. Snapshots of wavefields at 147 ms in a homogeneous medium. (a) Elastic VTI medium; (b) VTI medium with isotropic attenuation $Q_{P0} = Q_{S0} = 30$; (c) attenuative VTI medium with $Q_{P0} = Q_{S0} = 30$, $\epsilon_Q = 0$, $\delta_Q = 1.5$; (d) attenuative VTI medium with $Q_{P0} = Q_{S0} = 30$, $\epsilon_Q = 0.6$, $\delta_Q = 0$. (e) The difference between plots (b) and (c); and (f) the difference between plots (b) and (d). The model size is $1500 \text{ m} \times 1500 \text{ m}$, with grid spacing $\Delta x = \Delta z = 6 \text{ m}$. Other parameters are: $V_{P0} = 4000 \text{ m/s}$, $V_{S0} = 2000 \text{ m/s}$, $\epsilon = 0.3$, $\delta = 0.2$, and $\rho = 2.0 \text{ g/m}^3$. The phase velocities are defined at a reference frequency of 100 Hz. An explosive source that excites a Ricker wavelet with a central frequency of 100 Hz is placed at the center of the model.

Table 2. Parameters of a three-layer VTI model. The corresponding $\text{Re}(C_{ij})$ (related to the velocity parameters V_{P0} , V_{S0} , ϵ , and δ) are defined at a reference frequency of 100 Hz.

Layer	Thickness (km)	V_{P0} (km/s)	V_{S0} (km/s)	ϵ	δ	$\rho(\text{g/m}^3)$	Q_{P0}	Q_{S0}	ϵ_Q	δ_Q
1	0.2	2.0	1.0	0.15	0.1	2.0	30	30	-0.4	-1.2
2	0.2	3.0	1.5	0.2	0.15	2.2	30	30	-0.4	-1.2
3	0.2	4.0	2.0	0.3	0.2	2.5	30	30	-0.4	-1.2

pare the modeled traces with ones from the reference medium with isotropic attenuation (Figure 8). As expected, the difference becomes more pronounced with larger offset. More interestingly, because of negative parameters ε_Q and δ_Q , the energy is less attenuated at larger offsets despite a longer propagation path. This example illustrates the importance of taking attenuation anisotropy into account in AVO analysis (e.g., Samec and Blangy, 1992).

Finally, the anisotropic viscoelastic FD method is applied to a more complicated model with a salt body (Figure 9). This section is taken from the left part of the 2007 BP TTI model and is re-sampled with a coarser grid. We remove the tilt of the symmetry axis (i.e., turn the model into VTI) and make the section attenuative (Figure 10). The reflection energy is significantly damped due to attenuation (compare Figure 11b and 11c with Figure 11a). At large offsets (6–12 km), the diffraction from the left edge of the salt body (Figure 9a and 9b) interferes with reflections from the thin layers in the overburden (Figure 9c and 9d). This long-offset interference

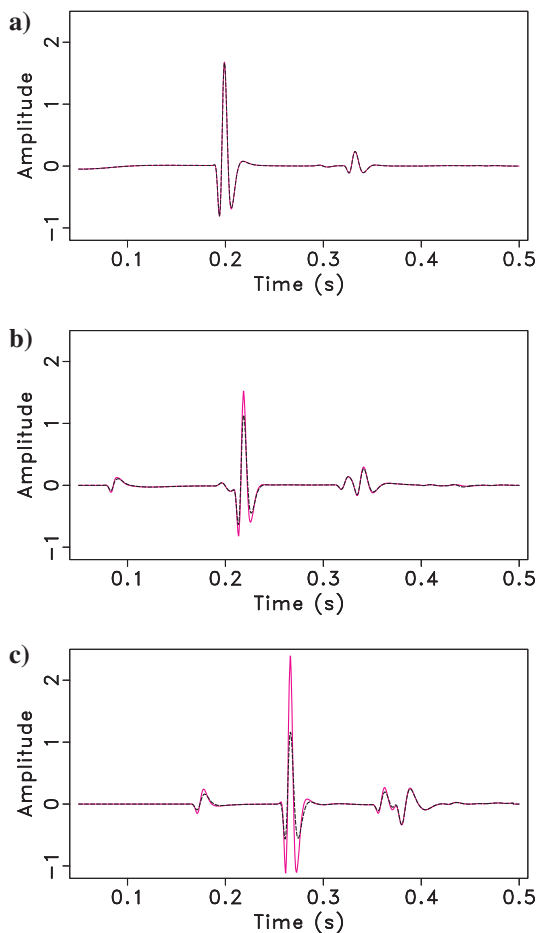


Figure 8. Traces of the vertical component of the reflection data (red solid lines) for the three-layer VTI model from Table 2. (a) The near-offset trace at $x = 0$ km; (b) the intermediate-offset trace at $x = 0.2$ km; (c) the far-offset trace at $x = 0.4$ km. The black dashed lines are modeling results for the same VTI medium but with isotropic attenuation (i.e., $\varepsilon_Q = \delta_Q = 0$). The model size is $400 \text{ m} \times 600 \text{ m}$, with grid spacing $\Delta x = \Delta z = 1 \text{ m}$.

arrival is significantly influenced by attenuation anisotropy in the shallow (0–3 km) layers (Figure 11d). Although attenuation anisotropy is also pronounced at depth, the difference between the amplitudes of the deeper events for the isotropic and VTI models is much smaller because of a more limited range of propagation angles. The spectra of windowed traces (Figure 12) exhibit the amplitude decay and reduction in the dominant frequency caused by attenuation anisotropy.

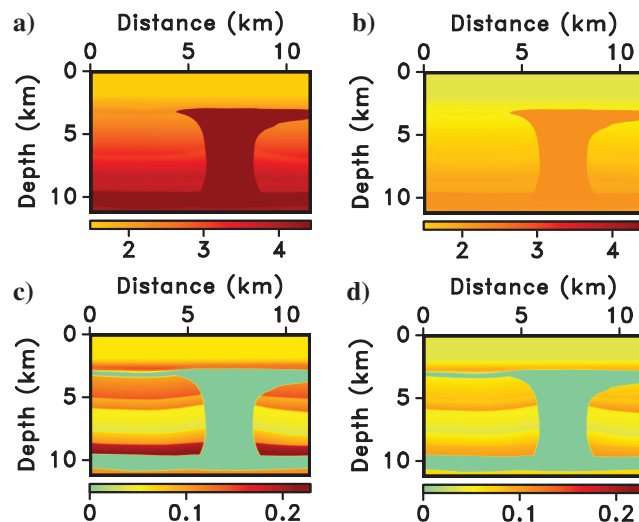


Figure 9. Velocity parameters of the salt section of the BP TI model: (a) V_{P0} , (b) V_{S0} (both velocities are in km/s), (c) ε , and (d) δ . The modified model size is $11268 \text{ m} \times 13125 \text{ m}$, with grid spacing $\Delta x = \Delta z = 18.75 \text{ m}$. An explosive source that excites a Ricker wavelet with a central frequency of 10 Hz is placed at the origin.

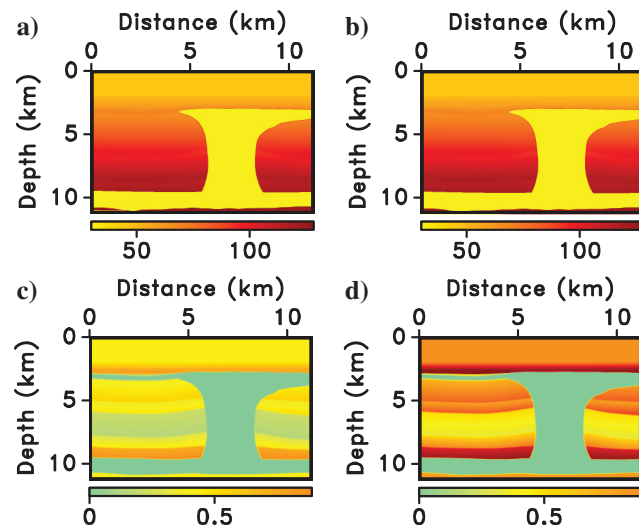


Figure 10. Attenuation parameters for the model from Figure 9: (a) Q_{P0} , (b) Q_{S0} , (c) ε_Q , and (d) δ_Q .

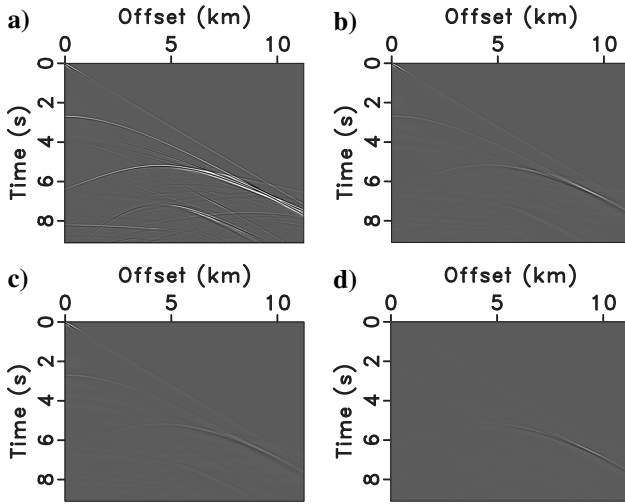


Figure 11. Vertical component of the reflection data for the model from Figures 9 and 10. The result of (a) elastic VTI modeling; (b) viscoelastic modeling with $\varepsilon_Q = \delta_Q = 0$; and (c) viscoelastic VTI modeling. (d) The difference between plots (b) and (c).

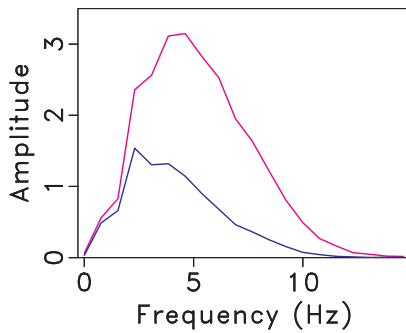


Figure 12. Spectra of windowed traces (from 6.3 s to 8.1 s) at an offset of 10.1 km for the model from Figures 9 and 10. The pink and blue curves correspond to the traces from Figure 11b and 11c, respectively.

CONCLUSIONS

We conducted time-domain FD modeling for 2D VTI attenuative media using the model of generalized standard linear solid (GSLs). The modified τ -method was employed to obtain the stress relaxation times and τ_{ij} -parameters and simulate nearly-constant Q_{ij} -behavior in a specified frequency range. The velocity dispersion produced by the GSLs model is close to that for Kjartansson's constant- Q model. Efficient numerical implementation is based on rotated staggered grids (RSG) and introduction of memory variables.

To validate the algorithm, we reconstructed the attenuation parameters of a VTI layer by applying the spectral-ratio method to the simulated reflection data. The method was also tested on a more structurally complex attenuative TI model that contains a salt body. The presented algorithm can serve as the forward-modeling tool for anisotropic attenuation tomography.

ACKNOWLEDGMENTS

We are grateful to the members of the A(nisotropy)-Team at CWP and John Anderson (ExxonMobil) for fruitful discussions.

The reviews by Josep de la Puente and two anonymous referees helped us improve the manuscript. This work was supported by the Consortium Project on Seismic Inverse Methods for Complex Structures at CWP. The reproducible numeric examples in this paper are generated with the Madagascar open-source software package freely available from <http://www.ahay.org>. Some of the codes are modified after the `sofi2D` package (<http://www.gpi.kit.edu/english/SOFI2D.php>).

APPENDIX A

VISCOELASTIC WAVE EQUATION FOR 2D VTI MEDIA

Here, we adopt the particle velocity-stress scheme to derive the viscoelastic wave equation for P- and SV-waves in 2D VTI media. A similar formalism is presented by Tromp et al. (2005) who employ the displacement-stress scheme and Fichtner and van Driel (2014) who choose a different definition of the memory variables.

Using the definition of τ_{ij} (equation 7), the relaxation function (equation 4) can be rewritten in the four-index notation as

$$\Psi_{mnpq}(t) = C_{mnpq}^R \left(1 + \frac{\tau_{mnpq}}{L} \sum_{l=1}^L e^{-t/\tau^{\sigma l}} \right) H(t), \quad (\text{A-1})$$

where there is no summation over the indices m, n, p and q .

Substituting equation A-1 into the generalized stress-strain relationship (equation 3) and then taking the time derivative on both sides yields:

$$\begin{aligned} \dot{\sigma}_{mn} &= \dot{\Psi}_{mnpq}(t) * \dot{\varepsilon}_{pq} \\ &= C_{mnpq}^U \dot{\varepsilon}_{pq} - \frac{1}{L} (C_{mnpq}^U - C_{mnpq}^R) \left(\sum_{l=1}^L \frac{e^{-t/\tau^{\sigma l}}}{\tau^{\sigma l}} \right) H(t) * \dot{\varepsilon}_{pq}; \end{aligned} \quad (\text{A-2})$$

here C_{mnpq}^U is the unrelaxed modulus defined as $C_{mnpq}^U = C_{mnpq}^R (1 + \tau_{mnpq})$.

Replacing the convolution terms with the memory variables r_{mn}^l , we transform equation A-2 into:

$$\dot{\sigma}_{mn} = \frac{1}{2} C_{mnpq}^U (v_{p,q} + v_{q,p}) + \sum_{l=1}^L r_{mn}^l, \quad (\text{A-3})$$

where

$$r_{mn}^l = -\frac{1}{L \tau^{\sigma l}} (C_{mnpq}^U - C_{mnpq}^R) e^{-t/\tau^{\sigma l}} H(t) * \dot{\varepsilon}_{pq}. \quad (\text{A-4})$$

Differentiating equation A-4 with respect to time, we find:

$$\begin{aligned} \dot{r}_{mn}^l &= -\frac{1}{\tau^{\sigma l}} \left[-\frac{1}{L \tau^{\sigma l}} (C_{mnpq}^U - C_{mnpq}^R) e^{-t/\tau^{\sigma l}} H(t) * \dot{\varepsilon}_{pq} \right] \\ &\quad - \frac{1}{L \tau^{\sigma l}} (C_{mnpq}^U - C_{mnpq}^R) e^{-t/\tau^{\sigma l}} \delta(t) * \dot{\varepsilon}_{pq}, \end{aligned} \quad (\text{A-5})$$

where $\delta(t)$ is the 1D δ -function.

Combining equations A-4 and A-5 yields the following differential equations:

$$\begin{aligned} \dot{r}_{mn}^l &= -\frac{1}{\tau^{\sigma l}} \left[\frac{1}{L} (C_{mnpq}^U - C_{mnpq}^R) \dot{\epsilon}_{pq} + r_{mn}^l \right] \\ &= -\frac{1}{\tau^{\sigma l}} \left[\frac{1}{2L} (C_{mnpq}^U - C_{mnpq}^R) (v_{p,q} + v_{q,p}) + r_{mn}^l \right], \quad (\text{A-6}) \end{aligned}$$

where $v_{p,q}$ is the derivative of the p th component of the particle velocity with respect to x_q ; the Einstein summation convention over p and q and Voigt convention are assumed.

Equations A-3 and A-6 describe viscoelastic wave propagation in VTI media. The relevant stress elements for P- and SV-waves in 2D VTI media are (the relaxed and unrelaxed moduli are expressed in the two-index Voigt notation):

$$\dot{\sigma}_{11} = C_{11}^U v_{1,1} + C_{13}^U v_{3,3} + \sum_{l=1}^L r_{11,l}, \quad (\text{A-7})$$

$$\dot{\sigma}_{33} = C_{13}^U v_{1,1} + C_{33}^U v_{3,3} + \sum_{l=1}^L r_{33,l}, \quad (\text{A-8})$$

$$\dot{\sigma}_{13} = C_{55}^U (v_{1,3} + v_{3,1}) + \sum_{l=1}^L r_{13,l}, \quad (\text{A-9})$$

with

$$\dot{r}_{11}^l = -\frac{1}{\tau^{\sigma l}} \left[\frac{1}{L} (C_{11}^U - C_{11}^R) v_{1,1} + \frac{1}{L} (C_{13}^U - C_{13}^R) v_{3,3} + r_{11}^l \right], \quad (\text{A-10})$$

$$\dot{r}_{33}^l = -\frac{1}{\tau^{\sigma l}} \left[\frac{1}{L} (C_{33}^U - C_{33}^R) v_{3,3} + \frac{1}{L} (C_{13}^U - C_{13}^R) v_{1,1} + r_{33}^l \right], \quad (\text{A-11})$$

$$\dot{r}_{13}^l = -\frac{1}{\tau^{\sigma l}} \left[\frac{1}{L} (C_{55}^U - C_{55}^R) (v_{3,1} + v_{1,3}) + r_{13}^l \right]. \quad (\text{A-12})$$

REFERENCES

Behura, J., and I. Tsvankin, 2009a, Estimation of interval anisotropic attenuation from reflection data: *Geophysics*, **74**, no. 6, A69–A74, doi: [10.1190/1.3191733](https://doi.org/10.1190/1.3191733).
 Behura, J., and I. Tsvankin, 2009b, Role of the inhomogeneity angle in anisotropic attenuation analysis: *Geophysics*, **74**, no. 6, WB177–WB191, doi: [10.1190/1.3230502](https://doi.org/10.1190/1.3230502).
 Blanch, J. O., J. O. Robertsson, and W. W. Symes, 1995, Modeling of a constant Q: Methodology and algorithm for an efficient and optimally inexpensive viscoelastic technique: *Geophysics*, **60**, 176–184, doi: [10.1190/1.1443744](https://doi.org/10.1190/1.1443744).
 Bohlen, T., 2002, Parallel 3-D viscoelastic finite difference seismic modelling: *Computers and Geosciences*, **28**, 887–899, doi: [10.1016/S0098-3004\(02\)00006-7](https://doi.org/10.1016/S0098-3004(02)00006-7).
 Carcione, J. M., 1993, Seismic modeling in viscoelastic media: *Geophysics*, **58**, 110–120, doi: [10.1190/1.1443340](https://doi.org/10.1190/1.1443340).

Carcione, J. M., 2007, *Wave fields in real media: Wave propagation in anisotropic, anelastic, porous and electromagnetic media*: Elsevier, 38.
 Červený, V., 2005, *Seismic ray theory*: Cambridge University Press.
 Charara, M., C. Barnes, and A. Tarantola, 2000, Full waveform inversion of seismic data for a viscoelastic medium, in P. C. Hansen, B. H. Jacobsen, and K. Mosegaard, eds., *Methods and Applications of Inversion*: Springer, 68–81.
 Day, S. M., and J. B. Minster, 1984, Numerical simulation of attenuated wavefields using a Pade approximant method: *Geophysical Journal International*, **78**, 105–118, doi: [10.1111/j.1365-246X.1984.tb06474.x](https://doi.org/10.1111/j.1365-246X.1984.tb06474.x).
 Emmerich, H., and M. Korn, 1987, Incorporation of attenuation into time-domain computations of seismic wave fields: *Geophysics*, **52**, 1252–1264, doi: [10.1190/1.1442386](https://doi.org/10.1190/1.1442386).
 Fichtner, A., and M. van Driel, 2014, Models and Fréchet kernels for frequency-(in) dependent Q: *Geophysical Journal International*, **198**, 1878–1889, doi: [10.1093/gji/ggu228](https://doi.org/10.1093/gji/ggu228).
 Futterman, W. L., 1962, Dispersive body waves: *Journal of Geophysical Research*, **67**, 5279–5291, doi: [10.1029/JZ0671013p05279](https://doi.org/10.1029/JZ0671013p05279).
 Gosselin-Cliche, B., and B. Giroux, 2014, 3D frequency-domain finite-difference viscoelastic-wave modeling using weighted average 27-point operators with optimal coefficients: *Geophysics*, **79**, T169–T188, doi: [10.1190/geo2013-0368.1](https://doi.org/10.1190/geo2013-0368.1).
 Hosten, B., M. Deschamps, and B. Tittmann, 1987, Inhomogeneous wave generation and propagation in lossy anisotropic solids: Application to the characterization of viscoelastic composite materials: *The Journal of the Acoustical Society of America*, **82**, 1763–1770, doi: [10.1121/1.395170](https://doi.org/10.1121/1.395170).
 Jacobson, R., 1987, An investigation into the fundamental relationships between attenuation, phase dispersion, and frequency using seismic refraction profiles over sedimentary structures: *Geophysics*, **52**, 72–87, doi: [10.1190/1.1442242](https://doi.org/10.1190/1.1442242).
 Kjartansson, E., 1979, Constant Q-wave propagation and attenuation: *Journal of Geophysical Research: Solid Earth (1978–2012)*, **84**, 4737–4748, doi: [10.1029/JB084iB09p04737](https://doi.org/10.1029/JB084iB09p04737).
 Komatitsch, D., and J. Tromp, 1999, Introduction to the spectral element method for three-dimensional seismic wave propagation: *Geophysical Journal International*, **139**, 806–822, doi: [10.1046/j.1365-246x.1999.00967.x](https://doi.org/10.1046/j.1365-246x.1999.00967.x).
 Kristek, J., and P. Moczo, 2003, Seismic-wave propagation in viscoelastic media with material discontinuities: A 3D fourth-order staggered-grid finite-difference modeling: *Bulletin of the Seismological Society of America*, **93**, 2273–2280, doi: [10.1785/0120030023](https://doi.org/10.1785/0120030023).
 Mittet, R., and L. Renlie, 1996, High-order, finite-difference modeling of multipole logging in formations with anisotropic attenuation and elasticity: *Geophysics*, **61**, 21–33, doi: [10.1190/1.1443942](https://doi.org/10.1190/1.1443942).
 Moczo, P., J. O. Robertsson, and L. Eisner, 2007, The finite-difference time-domain method for modeling of seismic wave propagation: *Advances in Geophysics*, **48**, 421–516, doi: [10.1016/S0065-2687\(06\)48008-0](https://doi.org/10.1016/S0065-2687(06)48008-0).
 Operto, S., J. Virieux, P. Amestoy, J.-Y. L'Excellent, L. Giraud, and H. B. H. Ali, 2007, 3D finite-difference frequency-domain modeling of visco-acoustic wave propagation using a massively parallel direct solver: A feasibility study: *Geophysics*, **72**, SM195–SM211, doi: [10.1190/1.2759835](https://doi.org/10.1190/1.2759835).
 Operto, S., J. Virieux, A. Ribodetti, and J. E. Anderson, 2009, Finite-difference frequency-domain modeling of viscoacoustic wave propagation in 2D tilted transversely isotropic (TTI) media: *Geophysics*, **74**, no. 5, T75–T95, doi: [10.1190/1.3157243](https://doi.org/10.1190/1.3157243).
 Robertsson, J. O., J. O. Blanch, and W. W. Symes, 1994, Viscoelastic finite-difference modeling: *Geophysics*, **59**, 1444–1456, doi: [10.1190/1.1443701](https://doi.org/10.1190/1.1443701).
 Saenger, E. H., and T. Bohlen, 2004, Finite-difference modeling of viscoelastic and anisotropic wave propagation using the rotated staggered grid: *Geophysics*, **69**, 583–591, doi: [10.1190/1.1707078](https://doi.org/10.1190/1.1707078).
 Saenger, E. H., N. Gold, and S. A. Shapiro, 2000, Modeling the propagation of elastic waves using a modified finite-difference grid: *Wave Motion*, **31**, 77–92, doi: [10.1016/S0165-2125\(99\)00023-2](https://doi.org/10.1016/S0165-2125(99)00023-2).
 Samec, P., and J. Blangy, 1992, Viscoelastic attenuation, anisotropy, and AVO: *Geophysics*, **57**, 441–450, doi: [10.1190/1.1443258](https://doi.org/10.1190/1.1443258).
 Shekar, B., and I. Tsvankin, 2011, Estimation of shear-wave interval attenuation from mode-converted data: *Geophysics*, **76**, no. 6, D11–D19, doi: [10.1190/geo2010-0415.1](https://doi.org/10.1190/geo2010-0415.1).
 Shekar, B., and I. Tsvankin, 2014, Kirchhoff modeling for attenuative anisotropic media using Gaussian beams: *Geophysics*, **79**, no. 5, WB51–WB61, doi: [10.1190/geo2013-0432.1](https://doi.org/10.1190/geo2013-0432.1).
 Sun, L. F., B. Milkereit, and D. R. Schmitt, 2009, Measuring velocity dispersion and attenuation in the exploration seismic frequency band: *Geophysics*, **74**, no. 2, WA113–WA122, doi: [10.1190/1.3068426](https://doi.org/10.1190/1.3068426).
 Tarantola, A., 1988, Theoretical background for the inversion of seismic waveforms including elasticity and attenuation: *Pure and Applied Geophysics*, **128**, 365–399, doi: [10.1007/BF01772605](https://doi.org/10.1007/BF01772605).
 Tromp, J., C. Tape, and Q. Liu, 2005, Seismic tomography, adjoint methods, time reversal and banana-doughnut kernels: *Geophysical Journal International*, **160**, 195–216, doi: [10.1111/j.1365-246X.2004.02453.x](https://doi.org/10.1111/j.1365-246X.2004.02453.x).
 Tsvankin, I., 2012, Seismic signatures and analysis of reflection data in anisotropic media: SEG.

- Vavryčuk, V., 2007, Ray velocity and ray attenuation in homogeneous anisotropic viscoelastic media: *Geophysics*, **72**, no. 6, D119–D127, doi: [10.1190/1.2768402](https://doi.org/10.1190/1.2768402).
- Zhu, T., J. M. Carcione, and J. M. Harris, 2013, Approximating constant-Q seismic propagation in the time domain: *Geophysical Prospecting*, **61**, 931–940, doi: [10.1111/1365-2478.12044](https://doi.org/10.1111/1365-2478.12044).
- Zhu, Y., and I. Tsvankin, 2006, Plane-wave propagation in attenuative transversely isotropic media: *Geophysics*, **71**, no. 2, T17–T30, doi: [10.1190/1.2187792](https://doi.org/10.1190/1.2187792).
- Zhu, Y., I. Tsvankin, P. Dewangan, and K. V. Wijk, 2007, Physical modeling and analysis of P-wave attenuation anisotropy in transversely isotropic media: *Geophysics*, **72**, no. 1, D1–D7, doi: [10.1190/1.2374797](https://doi.org/10.1190/1.2374797).